



LAWRENCE  
LIVERMORE  
NATIONAL  
LABORATORY

# Identifying External Influences on Global Precipitation

K. Marvel, C. Bonfils

July 18, 2013

Proceedings of the National Academy of Sciences of the  
United States of America

## **Disclaimer**

---

This document was prepared as an account of work sponsored by an agency of the United States government. Neither the United States government nor Lawrence Livermore National Security, LLC, nor any of their employees makes any warranty, expressed or implied, or assumes any legal liability or responsibility for the accuracy, completeness, or usefulness of any information, apparatus, product, or process disclosed, or represents that its use would not infringe privately owned rights. Reference herein to any specific commercial product, process, or service by trade name, trademark, manufacturer, or otherwise does not necessarily constitute or imply its endorsement, recommendation, or favoring by the United States government or Lawrence Livermore National Security, LLC. The views and opinions of authors expressed herein do not necessarily state or reflect those of the United States government or Lawrence Livermore National Security, LLC, and shall not be used for advertising or product endorsement purposes.

# Identifying External Influences on Global Precipitation

Kate Marvel \*, Céline Bonfils \*

\*Lawrence Livermore National Laboratory, Livermore, USA

Submitted to Proceedings of the National Academy of Sciences of the United States of America

**Changes in global (ocean and land) precipitation are among the most important and least well understood consequences of climate change. Increasing greenhouse gas concentrations are thought to affect the zonal-mean distribution of precipitation through two basic mechanisms. First, increasing temperatures will lead to an intensification of the hydrological cycle (“thermodynamic” changes). Second, changes in atmospheric circulation patterns will lead to poleward displacement of the storm tracks and subtropical dry zones and to a widening of the tropical belt (“dynamic” changes). We demonstrate that both these changes are occurring simultaneously in global precipitation, that this behavior cannot be explained by internal variability alone, and that external influences are responsible for the observed precipitation changes. While existing model experiments are not of sufficient length to differentiate between natural and anthropogenic forcing terms at the 95% confidence level, we present evidence that the observed trends result from human activities.**

## Significance Statement

This study provides evidence that human activities are affecting precipitation over land and oceans. Anthropogenic increases in greenhouse gases and stratospheric ozone depletion are expected to lead to a latitudinal intensification and redistribution of global precipitation. However, detecting these mechanisms in the observational record is complicated by strong climate noise and model errors. By introducing new methods, we establish for the first time that the changes in land and ocean precipitation predicted by theory are indeed present in the observational record, that these changes are unlikely to arise purely due to natural climate variability, and that external influences, probably anthropogenic in origin, are responsible.

climate change | detection and attribution | climate modeling | precipitation

**W**ater is the single most important natural resource, and many societal and natural impacts of climate change will depend on the response of the hydrological cycle to anthropogenic warming. Several large-scale changes in precipitation, inferred from theoretical understanding, observations and climate model predictions, are expected in a warming world [1]. To first order, anthropogenic forcings are expected to influence the hydrological cycle through two basic mechanisms. *Thermodynamic* changes follow from the Clausius-Clapeyron (CC) relation, which dictates that saturation specific humidity increases roughly exponentially with temperature, and from the vertical warming profile [2, 3]. In the absence of other changes, this increase in tropospheric water vapor will make wet regions wetter and dry regions drier. Tropospheric water vapor is indeed increasing in response to human activities [4], and there is evidence that this increase has contributed to the moistening of wet regions and drying of dry regions [5, 6, 7]. Existing large-scale studies [7, 8, 9] are constrained over land, and thus neglect the 77% of precipitation that falls over oceans. Thermodynamic changes are expected to be even stronger over ocean, because evaporation is limited over dry land regions, and trends in ocean salinity may indicate an intensification of the global hydrological cycle

[10]. However, no study has yet detected a signal of climate change in global (land and ocean) precipitation.

*Dynamic* changes result from shifts in atmospheric circulation, which in turn affect the horizontal and vertical transport of water vapor. Numerous observational and model-based studies have detected circulation shifts using various metrics (see [11] and references therein). Models indicate that increasing greenhouse gases, in the absence of other external forcing terms, result in a poleward expansion of the tropical Hadley cell and subtropical dry zones [12]. However, stratospheric ozone depletion can also lead to similar circulation shifts [13] and is likely the dominant contributor to the observed poleward movement in Southern Hemisphere circulation patterns in austral summer [14].

Any study of anthropogenic influences on global precipitation must therefore consider both thermodynamic and dynamic mechanisms [15]. Detection of the climate change signal is complicated by the muted response of global-mean model precipitation to a temperature increase (compared to the increase in water vapor) and the zonal nature of the predicted changes (in both sign and displacement). Additional difficulties exist: first, it is well known that interannual and interdecadal modes of natural variability such as the El Niño/Southern Oscillation (ENSO) have considerable impacts on precipitation, potentially obscuring any climate change signal. Second, global precipitation climatologies exhibit strong spatial gradients, and model errors in representing the locations of these gradients are common. Consequently, averaging precipitation over latitude bands and over many simulations (as in [7, 9]), which is generally performed to reduce the influence of internal variability, may also obscure physically robust simulated precipitation shifts. Finally, total precipitation is also strongly influenced by orography, cloud formation, and other small-scale processes that may not be well-simulated in climate models.

In this paper, we argue that the presence of two physically robust, interlinked mechanisms necessitates the use of multivariate detection techniques [16]. We propose a method to simultaneously detect the intensification and latitudinal redistribution of global precipitation, test these changes against model estimates of natural internal variability, and investigate the roles of various relevant external forcings.

## Reserved for Publication Footnotes

## Thermodynamic and Dynamic Indicators

We use the Global Precipitation Climatology Project (GPCP) global observational dataset [17] spanning 1979–2012. In this paper, we focus on boreal winter (December–February; hereafter DJF). We begin by smoothing observed DJF seasonal precipitation climatologies so that spatial structure on scales less than  $5^\circ$  is removed [18], Figure 1(a) shows the result of this smoothing process for a single representative year (1990). The smoothed, zonally averaged precipitation field has five local extrema, excluding the polar-most points. Physically, these correspond to (from left), the Southern Hemisphere (SH) mid-latitude storm track peak, SH subtropical dry zone trough, equatorial tropical peak, Northern Hemisphere (NH) dry zone trough, and NH storm track peak. In the observations, the zonally averaged smoothed DJF precipitation has exactly five local extrema in every year.

For each year, we calculate the latitude and intensity (i.e., the value of the smoothed precipitation field) at each extremum. We then calculate the six “half max” latitude points, defined as the latitudes where the smoothed zonally averaged precipitation is equal to the average of the nearest peak and trough. This process yields 1) a dynamic time series  $D_o(t)$  with 11 spatial dimensions representing variations in peak, trough, and half max latitudes, and 2) a thermodynamic time series  $T_o(t)$  with 5 spatial dimensions representing variations in the intensity at each peak and trough<sup>1</sup>. We then calculate the anomalies  $D'_o(t)$  (Figure 1b) and  $T'_o(t)$  (Figure 1c) relative to 1980–2012 observed time means. This allows us to characterize total changes in zonally averaged precipitation using intensification and shifts simultaneously.

We apply the same methods to climate model precipitation data from the 3rd and 5th phases of the Coupled Model Intercomparison Project (CMIP3/CMIP5). In order to obtain model data spanning the observational period, we splice together the “historical” and “RCP 8.5” or “A1B” projection experiments (SI Appendix: Section S2). For each model, we perform the same smoothing and peak detection procedure. Anomalies  $D'_H(t)$  and  $T'_H(t)$  are now calculated with respect to the *model* 1980–2012 average peak/trough and half max latitude and intensity. This technique effectively preserves and highlights the changes in intensity and displacement that likely would be obscured in the multimodel average of zonal mean precipitation. The procedure is then repeated for yearly seasonal DJF climatologies in the CMIP5 pre-industrial control (PIC) runs, yielding control anomaly time series  $D'_C(t)$  and  $T'_C(t)$ , which are then concatenated into a single time series (SI Appendix: Section S1).

## Fingerprints

We estimate the expected response of the dynamic and thermodynamic indicators to external forcing using a leading “fingerprint” method [16, 19]. We begin by first averaging the anomaly time series  $D'_H(t)$  and  $T'_H(t)$  over an individual model’s spliced historical and RCP8.5 realizations, and then averaging over all models. Because internal variability is uncorrelated across models, this reduces the effect of climate noise, yielding a clearer picture of the climate system’s response to external forcing: the “fingerprint” of climate change.

To examine simultaneous thermodynamic and dynamic changes, we calculate the leading multivariate empirical orthogonal function (EOF)  $F_m(D, T)$ , determined from the cross-covariance matrix of the multimodel average  $\overline{D'_H(t)}$  and  $\overline{T'_H(t)}$  (Fig 2a). This fingerprint reveals that the multimodel response of the climate system to external forcing is characterized by two physical effects: a wet-get-wetter, dry-get-drier

pattern in precipitation intensity, and an attendant poleward expansion in both hemispheres in zonal mean precipitation. The associated first principal component (PC) (Figure 2b) shows a distinct positive trend over the observational time period. By contrast, Figure 2c shows the leading noise EOF of the concatenated PIC runs, and Figure 2d the associated PC. This EOF resembles the fingerprint  $F_m(D, T)$  except, instead of the poleward expansion observed in the forced case, it displays the equatorial *contraction* expected in the zonal mean response to ENSO [20, 21]. This suggests that ENSO, the primary mode of natural variability, will not project well onto the multivariate fingerprint  $F_m(D, T)$ . In other words, using this fingerprint will improve signal-to-noise ratios by effectively filtering out climate noise (SI Appendix: Section S8).

Even though both thermodynamic and dynamic responses are based in fundamental physics, and therefore robust across multiple independent climate models, model errors may mask even strong responses. The fingerprint, or characteristic response to external forcing, is often obtained by averaging over multiple models to eliminate internal variability. This response may be diluted if models disagree on the locations of important features. For example, two models projecting strong subtropical drying trends may yield a smaller trend when averaged if the model dry zones are sufficiently far apart. Additionally, estimates of internal variability are often obtained by concatenating the pre-industrial control runs of multiple models into a single long time series. However, variations in the principal components of the concatenated control runs may reflect model biases, not the amplitude of internal variability in the models. Previous attempts to control for model errors have included coarse zonal averaging [7], focus on a single region [5, 6], the use of a warping function for feature bias correction [22], and the model-by-model approach described in [23]. The method we employ (SI Appendix: Section S4) is designed to capitalize on robust model features even in the presence of feature biases. This method allows for the simultaneous detection of dynamic and thermodynamic changes in zonal mean precipitation and demonstrates that these changes are inconsistent with internal climate variability, as we now show.

## Detection of Changes

To determine if these changes in intensity and location are present in the observations, we project the combined observed anomaly fields  $D'_O(t)$  and  $T'_O(t)$ , normalized to unit variance, onto the multivariate fingerprint  $F_m(D, T)$ . This projection yields the spatial covariance between the observed pattern and the fingerprint at time  $t$  and measures the similarity between the observed and fingerprint patterns. If the externally forced fingerprint is present and growing in the observations, then the projection should increase with time and display an overall positive trend [19]. By contrast, the fingerprint should not be expressed in precipitation changes originating from climate noise alone, except by chance. We use this characteristic to assess whether observed trends can be explained by internal variability. To do so, we calculate the distribution of 33-year non-overlapping trends in the concatenated model PIC projections onto the fingerprint  $F_m(D, T)$ . The standard deviation of this distribution, denoted  $\epsilon$ , constitutes a measure of internal climate variability. The signal-to-noise (S/N) ratio is then obtained by dividing the observed trend by  $\epsilon$ .

<sup>1</sup> The terminology used here represents an oversimplification: dynamical shifts can also contribute to changes in precipitation intensity, while large-scale changes in precipitation may have consequences for atmospheric circulation.

If observed trends are incompatible with internal variability, we can claim to have “detected” a signal. To “attribute” a detected signal to external forcing, we need to assess whether it is compatible with forced model results. While all models in the CMIP5 archive incorporate the effects of ozone depletion in addition to other human and natural forcings, only half of those in the previous generation (CMIP3) do so [14]. This allows us to determine the relative weight of GHG and ozone contributions to changes in precipitation. We therefore calculate the projections onto the fingerprint for the spliced CMIP5 models (ALL5), and spliced CMIP3 models including (ALL3) or excluding (NoOz3) anthropogenic stratospheric ozone depletion.

Figure 3a shows the projection of the observed dynamic and thermodynamic indicators, normalized to unit variance, onto the fingerprint  $F_m(D, T)$ . The corresponding signal-to-noise ratio is shown in Figure 3b, as well as fitted probability density functions for the PIC, ALL5, ALL3, and NoOz3 S/N ratios. A strong positive trend is evident in the observed projection. As expected, the distribution of 33-year non-overlapping control run trends is centered around zero. The observed S/N ratio of 2.4 is well above the 5% significance threshold, suggesting that the observed co-variability between location and intensity is incompatible with internal climate noise alone. The ALL3 and ALL5 trends do not differ significantly from each other, nor do they differ from the NoOz distribution (Table S1). The observed S/N ratio is located near the mean of all three externally forced distributions. This indicates that the combined amplification and shift in zonal precipitation is externally forced and present even in the absence of anthropogenic ozone depletion.

To differentiate between natural and anthropogenic forcing terms, we repeated the analysis over the shorter time period spanned by the “historicalNat” experiments in the CMIP5 database (1980-2005). These experiments incorporate solar variability and volcanic eruptions over the historical period, but contain no anthropogenic forcings. The results, now using 26-year trends, are shown in Figure 3c. The observed trend lies in the tail of the historicalNat and pi-Control distributions, but the S/N ratio is not significant at the 95% confidence level. This is likely due to the shortened period over which we calculate trends. However, the similarity between the historicalNat trend distribution and the PIC trend distribution, and the fact that these distributions significantly differ from those obtained using anthropogenically forced models, strongly suggest that natural external forcings alone are unlikely to explain the observed changes.

## Modeled Internal Variability

Detection and attribution studies rely on credible model estimates of internal variability [24, 25]. If models systematically underestimate the amplitude of natural climate noise, this may lead to spurious detection due to artificially low variability inflating the signal-to-noise ratio. It is therefore important to compare variability in observations and spliced CMIP5 historical/RCP8.5 runs. We first detrend modeled and observed time series of projections onto the multivariate  $F_m(D, T)$  fingerprint and then apply a band-pass filter to extract variability on scales between 5 and 20 years, as in [25]. We also apply a high-pass filter to extract variability on scales less than three years. Figure 4a shows the performance of models at simulating medium and high-frequency variability in the projection. Model estimates of decadal variability are more important for D&A applications, and Figure 4a indicates a systematic underestimate in decadal variability of the

multivariate projection. Does this lead to spurious detections by inflating the S/N ratio? To investigate this possibility, we consider only those models (FGOALS-s2 and MIROC-ESM-CHEM) in which the *ensemble average* over realizations overestimates 5-20 year variability in the multivariate projection. Restricting our analysis to these two models only, we find (Figure 4b) that the observed trend is still highly unlikely to occur in these model control runs at the 95% confidence level.

## Comparisons with previous work

It is important to note that our detection method relies on the covariance matrix measuring the relationship between the dynamic and thermodynamic indicators. In order to calculate the fingerprint and projection, we normalize each indicator to unit variance, thus removing information about the amplitude of variability in the individual components. Our fingerprint therefore measures the degree of synchronicity between variations in the thermodynamic and dynamic indicators, not their respective amplitudes. This means it is possible to detect a trend in the projection onto  $F_m(D, T)$  in the absence of trends in either  $D_o(t)$  or  $T_o(t)$ , if thermodynamic changes and dynamic changes increasingly occur in tandem.

It is, of course, possible to calculate single-variable fingerprints to examine changes in  $D_o(t)$  (SI Appendix, Section S6.1) or  $T_o(t)$  (SI Appendix, Section S6.2) separately. The noise filtering aspect of the multivariate fingerprint is lost in the single-variable cases: natural variability, ENSO in particular, will project onto these fingerprints and decrease the signal-to-noise ratio (SI Appendix: Figure S8). However, considering each variable separately allows for comparisons with previous studies that have detected changes in the hydrological cycle or atmospheric circulation.

We find, considering the dynamical indicator alone, that the observations do show a poleward shift in the main features of global precipitation. As previous authors [14] have found, the observed trend is much larger than the trends found in forced model runs, although including anthropogenic stratospheric ozone depletion reduces the discrepancy.

Although other studies [7, 26] have found evidence for thermodynamic changes in the hydrological cycle, we do not detect a trend in the thermodynamic indicator alone. This is due to differences in datasets and time periods considered (SI Appendix: Figures S4-6). Our method is designed to detect changes in the zonal-mean structure of global precipitation; other metrics, designed to capture more local changes, have found evidence for regional thermodynamic changes [27] that exceed model predictions.

## Conclusions

In this paper, we have introduced a simple new method to track thermodynamic and dynamic changes in global precipitation. This method identifies physical effects that are robust across multiple models, even in the presence of model errors. We have identified a fingerprint pattern that characterizes the simultaneous response of precipitation location and intensity to external forcing and acts as a noise filter. Observed changes in this multivariate response are incompatible with our best estimates of natural variability and consistent with model predictions of externally forced change. The synchronicity of these changes is key, however: considering either change in isolation does not lead to detection *and* attribution (SI Appendix: Figure S3). By focusing on *both* the underlying mechanisms that drive changes in global precipitation, and by restricting our analysis to the large scales where we have some confidence in models’ ability to reproduce the current climate,

we have shown that the changes observed in the satellite era are externally forced, and likely to be anthropogenic in nature.

**ACKNOWLEDGMENTS.** We are very grateful to Ben Santer and Karl Taylor for helpful comments and infinite patience. This work was supported by the Global Climate Modeling Program of the U.S. Department of Energy (DOE) Office of Science and was performed under the auspices of the U.S. DOE Lawrence Livermore National Laboratory (Contract DE-AC52-07NA27344). K.M. was supported by an

LLNL LDRD award. C.B. was supported by her DOE/OBER Early Career Research Program award. We acknowledge the World Climate Research Programme's Working Group on Coupled Modelling, which is responsible for CMIP, and we thank the climate modeling groups (listed in Table S2 of this paper) for producing and making available their model output. For CMIP the U.S. Department of Energy's Program for Climate Model Diagnosis and Intercomparison provides coordinating support and led development of software infrastructure in partnership with the Global Organization for Earth System Science Portals.

1. Stott, P. A., Gillett, N. P., Hegerl, G. C., Karoly, D. J., Stone, D. A., Zhang, X., & Zwiers, F. (2010) Detection and attribution of climate change: a regional perspective. *Wiley Interdisciplinary Reviews: Climate Change* 1, 192–211.
2. Allen, M. R. & Ingram, W. J. (2002) Constraints on future changes in climate and the hydrologic cycle. *Nature* 419, 224–232.
3. Held, I. M. & Soden, B. J. (2006) Robust responses of the hydrological cycle to global warming. *Journal of Climate* 19, 5686–5699.
4. Santer, B. D., Mears, C., Wentz, F., Taylor, K., Gleckler, P., Wigley, T., Barnett, T., Boyle, J., Brüggemann, W., Gillett, N., et al. (2007) Identification of human-induced changes in atmospheric moisture content. *Proceedings of the National Academy of Sciences* 104, 15248–15253.
5. Fyfe, J., Gillett, N., & Marshall, G. (2012) Human influence on extratropical southern hemisphere summer precipitation. *Geophysical Research Letters* 39.
6. Min, S.-K., Zhang, X., & Zwiers, F. (2008) Human-induced arctic moistening. *Science* 320, 518–520.
7. Zhang, X., Zwiers, F. W., Hegerl, G. C., Lambert, F. H., Gillett, N. P., Solomon, S., Stott, P. A., & Nozawa, T. (2007) Detection of human influence on twentieth-century precipitation trends. *Nature* 448, 461–465.
8. Noake, K., Polson, D., Hegerl, G., & Zhang, X. (2012) Changes in seasonal land precipitation during the latter twentieth-century. *Geophysical Research Letters* 39.
9. Polson, D., Hegerl, G. C., Zhang, X., & Osborn, T. J. (2013) Causes of robust seasonal land precipitation changes. *Journal of Climate*.
10. Durack, P. J., Wijffels, S. E., & Matear, R. J. (2012) Ocean salinities reveal strong global water cycle intensification during 1950 to 2000. *Science* 336, 455–458.
11. Seidel, D. J., Fu, Q., Randel, W. J., & Reichler, T. J. (2007) Widening of the tropical belt in a changing climate. *Nature Geoscience* 1, 21–24.
12. Shindell, D. T. & Schmidt, G. A. (2004) Southern hemisphere climate response to ozone changes and greenhouse gas increases. *Geophysical Research Letters* 31.
13. Kang, S., Polvani, L., Fyfe, J., & Sigmond, M. (2011) Impact of polar ozone depletion on subtropical precipitation. *Science* 332, 951–954.
14. Min, S.-K. & Son, S.-W. (2013) Multi-model attribution of the southern hemisphere Hadley cell widening: Major role of ozone depletion. *Journal of Geophysical Research: Atmospheres*.
15. Seager, R., Naik, N., & Vecchi, G. A. (2010) Thermodynamic and dynamic mechanisms for large-scale changes in the hydrological cycle in response to global warming. *Journal of Climate* 23, 4651–4668.
16. Santer, B. D., Mikolajewicz, U., Brüggemann, W., Cubasch, U., Hasselmann, K., Höck, H., Maier-Reimer, E., & Wigley, T. M. (1995) Ocean variability and its influence on the detectability of greenhouse warming signals. *Journal of Geophysical Research* 100, 10693–10.
17. Adler, R. F., Huffman, G. J., Chang, A., Ferraro, R., Xie, P.-P., Janowiak, J., Rudolf, B., Schneider, U., Curtis, S., Bolvin, D., et al. (2003) The version-2 global precipitation climatology project (GPCP) monthly precipitation analysis (1979–present). *Journal of Hydrometeorology* 4, 1147–1167.
18. Marvel, K., Ivanova, D., & Taylor, K. (2013) Scale space methods for climate model analysis. *Journal of Geophysical Research: Atmospheres*.
19. Santer, B. D., Painter, J. F., Mears, C. A., Doutriaux, C., Caldwell, P., Arblaster, J. M., Cameron-Smith, P. J., Gillett, N. P., Gleckler, P. J., Lanzante, J., et al. (2013) Identifying human influences on atmospheric temperature. *Proceedings of the National Academy of Sciences* 110, 26–33.
20. Lu, J., Chen, G., & Frierson, D. M. (2008) Response of the zonal mean atmospheric circulation to El Niño versus global warming. *Journal of Climate* 21, 5835–5851.
21. Seager, R. & Naik, N. (2012) A mechanisms-based approach to detecting recent anthropogenic hydroclimate change. *Journal of Climate* 25, 236–261.
22. Levy, A. A., Ingram, W., Jenkinson, M., Huntingford, C., Hugo Lambert, F., & Allen, M. (2013) Can correcting feature location in simulated mean climate improve agreement on projected changes? *Geophysical Research Letters* 40, 354–358.
23. Scheff, J. & Frierson, D. (2012) Twenty-first-century multimodel subtropical precipitation declines are mostly midlatitude shifts. *Journal of Climate* 25, 4330–4347.
24. Allen, M. R. & Tett, S. F. (1999) Checking for model consistency in optimal fingerprinting. *Climate Dynamics* 15, 419–434.
25. Santer, B., Mears, C., Doutriaux, C., Caldwell, P., Gleckler, P., Wigley, T., Solomon, S., Gillett, N., Ivanova, D., Karl, T., et al. (2011) Separating signal and noise in atmospheric temperature changes: The importance of timescale. *Journal of Geophysical Research: Atmospheres* (1984–2012) 116.
26. Wentz, F. J., Ricciardulli, L., Hilburn, K., & Mears, C. (2007) How much more rain will global warming bring? *Science* 317, 233–235.
27. Allan, R. P., Soden, B. J., John, V. O., Ingram, W., & Good, P. (2010) Current changes in tropical precipitation. *Environmental Research Letters* 5, 025205.

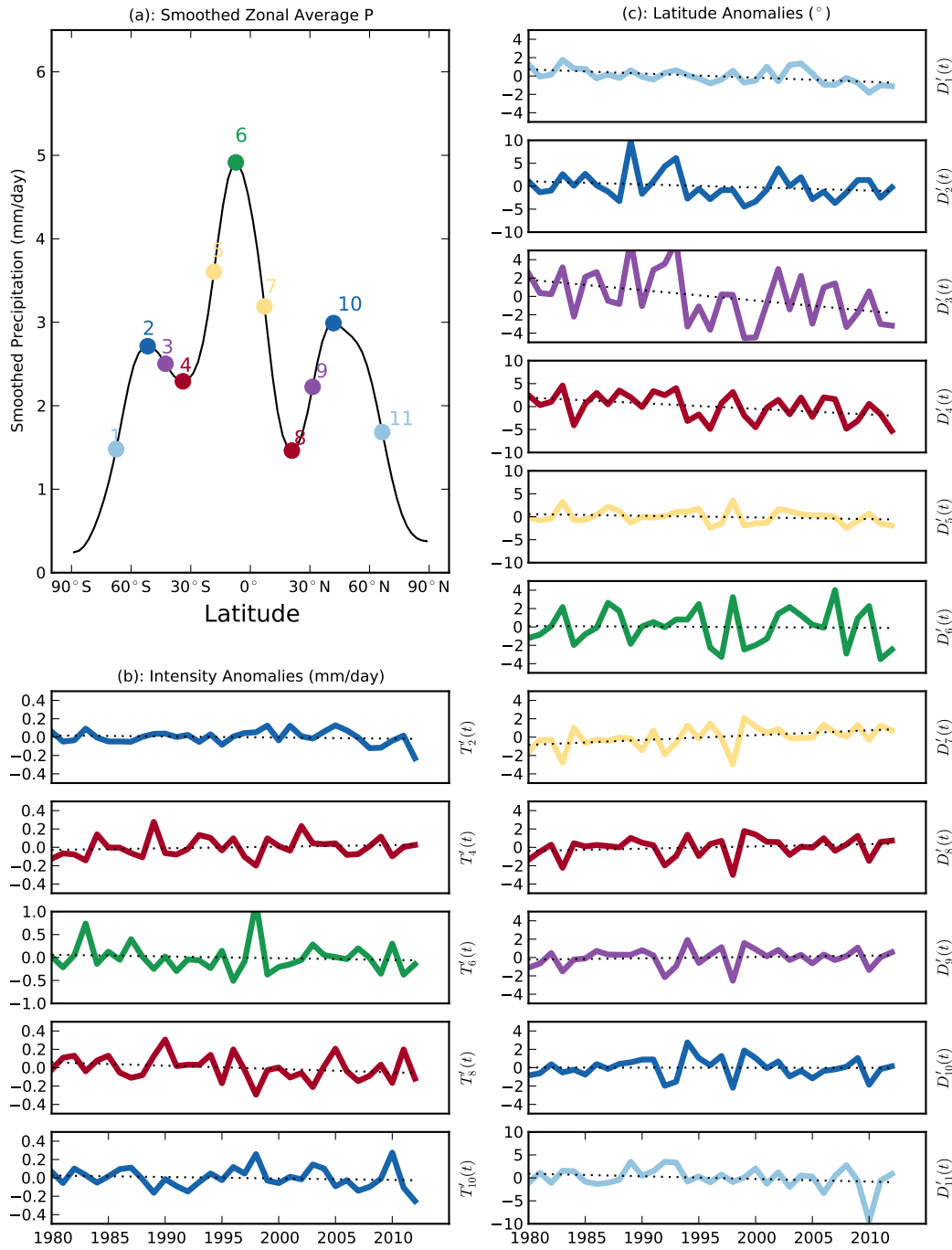


**Fig. 1.** Illustration of the methods used to generate thermodynamic and dynamic indicators. (a) Smoothed, zonally averaged boreal winter precipitation in the observational GPCP dataset for 1990. Local extrema are marked in dark blue (mid-latitude storm tracks), red (subtropical dry zones), and green (equatorial tropical peak). Cyan, purple, and yellow circles indicate "half-max" points: latitudes where the smoothed zonally averaged precipitation is equal to the average of neighboring extrema. (b) Observed peak "intensity" anomalies (mm/day) in the observational dataset. Best-fit trends obtained by linear regression are shown as black dotted lines. (c) Observed peak and halfmax point location anomalies in the observational dataset. Best-fit trends are drawn as black dotted lines.

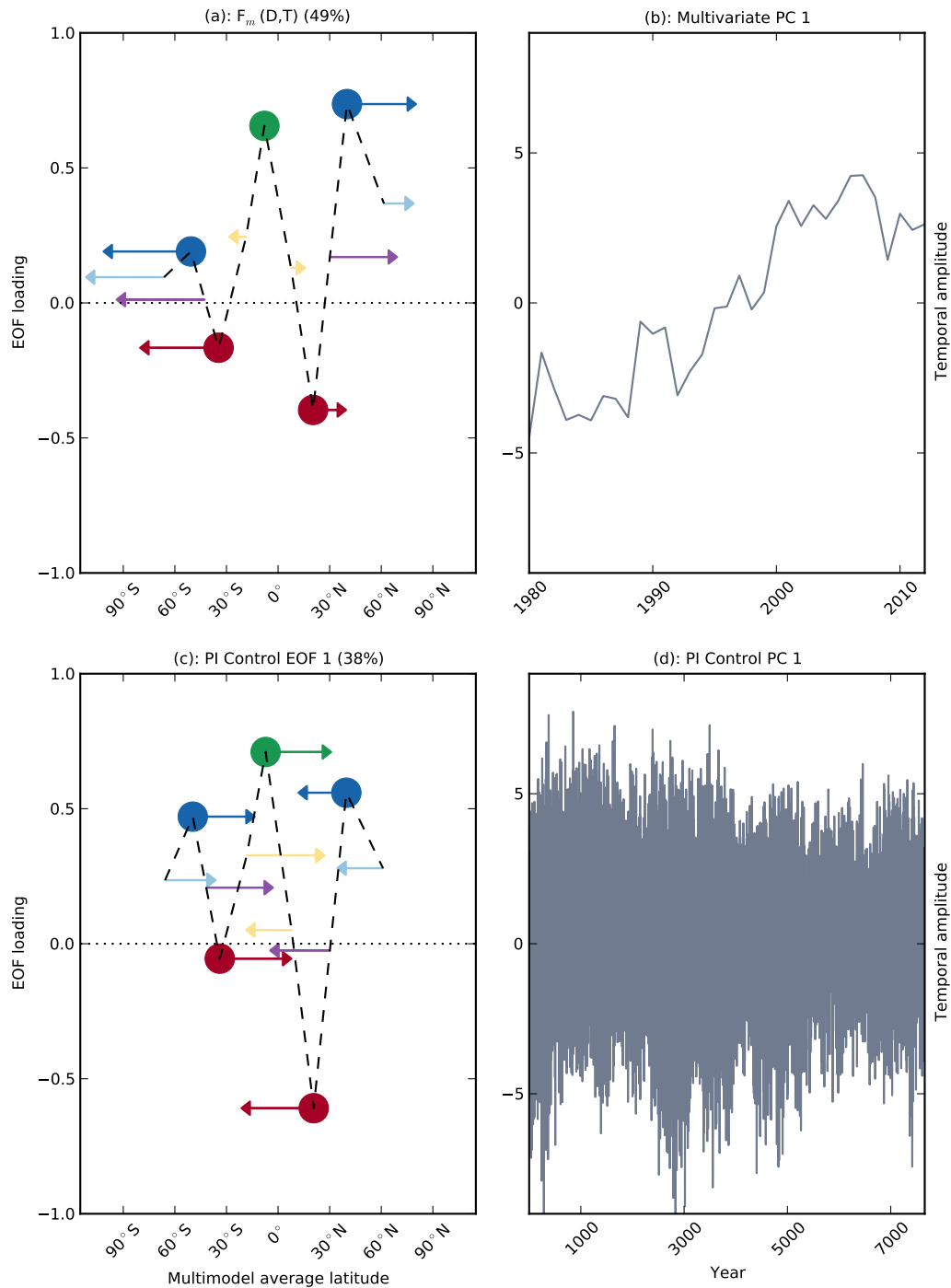


**Fig. 2.** The multivariate “fingerprint” of forced precipitation change and the primary noise mode. (a) The fingerprint  $F_m(D,T)$ , or leading eigenvector of the cross-covariance matrix of the multimodel average  $\overline{D'_H(t)}$  and  $\overline{T'_H(t)}$ . Both time series are scaled to unit variance before input. Thermodynamic EOF loading is plotted on the vertical axis, while the direction and magnitude of dynamic EOF loading are displayed as arrows. The horizontal axis is the multimodel average latitude of detected peak/trough and halfmax points. For visual clarity the arrows exaggerate the actual shift in latitude by a factor of 50. This EOF explains 49% of the total variance. (b) The principal component associated with the fingerprint  $F_m(D,T)$ . (c) The leading noise eigenvector of the cross-covariance matrix of the concatenated model PIC runs  $D'_C(t)$  and  $T'_C(t)$ . As in (a), the y-axis shows thermodynamic EOF loading, while arrows, scaled by a factor of 50, show dynamic EOF loading. The x-axis shows the multimodel average latitude of detected points. This EOF explains 38% of the total variance. (d) The principal component associated with the leading noise EOF.



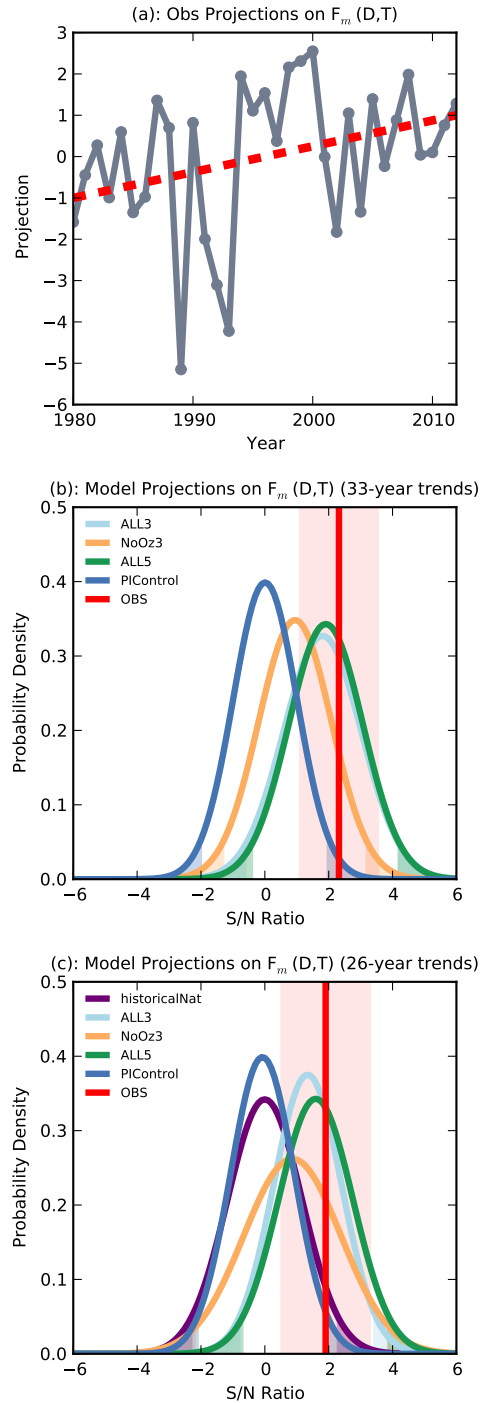


**Fig. 3.** (a) The projection (gray) of the observed thermodynamic and dynamic indicators onto the multivariate fingerprint, and best-fit line (red). (b) Best-fit normal probability distribution functions (PDFs) for trends in the projection of model data onto the fingerprint. All trends have been normalized by  $\epsilon$ , the standard error of the control distribution to obtain signal-to-noise ratios. The blue line shows the PDF of non-overlapping 33-year trends from the concatenated model PIC runs. The green line shows the PDF for individual CMIP5 historical/RCP8.5 model projection trends. Yellow/cyan lines show the PDF for CMIP3 models excluding/including stratospheric ozone depletion. For all PDFs, the two-sided 95% confidence intervals are shaded. The red line indicates the observed S/N ratio, and the shaded red box  $\pm$  one standard error in estimating the trend from assumed independent annual samples. The observed S/N ratio, located near the mean of the forced distributions, is incompatible with internal variability at 95% confidence. (c) As in Figure 3b, but for 26-year trends and including “historicalNat” experiments. The observed S/N ratio is located near the mean of the forced distributions and in the tail of both control and historicalNat distributions.

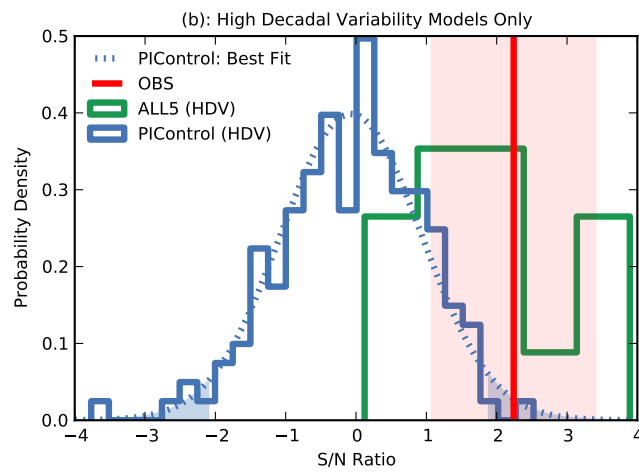
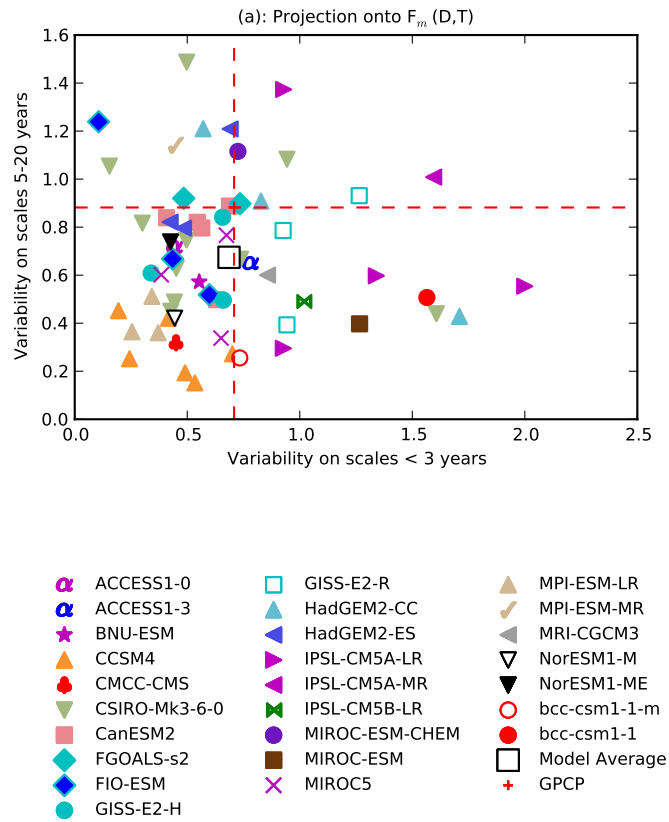


**Fig. 4.** (a) Comparison of modeled and observed variability in the multivariate projection onto the fingerprint  $F_m(D,T)$ . (b) Normalized histograms of trends in the multivariate projection onto the fingerprint  $F_m(D,T)$  for the control runs (blue) and spliced historical and RCP8.5 runs, considering only models that overestimate decadal variability in the projection ("high decadal variability" or HDV models.)